Engineering Science and Technology, an International Journal xxx (2016) xxx–xxx

HOSTED BY

ELSEVIER

Contents lists available at ScienceDirect

Engineering Science and Technology, an International Journal

journal homepage: www.elsevier.com/locate/jestch

Full Length Article

A quadrilateral inverse-shell element with drilling degrees of freedom for shape sensing and structural health monitoring

Adnan Kefal [a], Erkan Oterkus [a,*], Alexander Tessler [b], Jan L. Spangler [c]

[a] Department of Naval Architecture, Ocean and Marine Engineering, University of Strathclyde, 100 Montrose Street, Glasgow G4 0LZ, United Kingdom
[b] Structural Mechanics and Concepts Branch, NASA Langley Research Center, Mail Stop 190, Hampton, VA 23681-2199, USA
[c] Lockheed Martin Aeronautics Company, NASA Langley Research Center, Mail Stop 190, Hampton, VA 23681-2199, USA

ARTICLE INFO

Article history:
Received 15 September 2015
Revised 3 March 2016
Accepted 7 March 2016
Available online xxxx

Keywords:
Structural health monitoring
Inverse Finite Element Method
Shell structures

ABSTRACT

The inverse Finite Element Method (iFEM) is a state-of-the-art methodology originally introduced by Tessler and Spangler for real-time reconstruction of full-field structural displacements in plate and shell structures that are instrumented by strain sensors. This inverse problem is commonly known as shape sensing. In this effort, a new four-node quadrilateral inverse-shell element, iQS4, is developed that expands the library of existing iFEM-based elements. This new element includes hierarchical drilling rotation degrees-of-freedom (DOF) and further extends the practical usefulness of iFEM for shape sensing analysis of large-scale structures. The iFEM/iQS4 formulation is derived from a weighted-least-squares functional that has Mindlin theory as its kinematic framework. Two validation problems, (1) a cantilevered plate under static transverse force near the free tip, and (2) a short cantilever beam under shear loading, are solved and discussed in detail. Following the validation cases, the applicability of the iQS4 element to more complex structures is demonstrated by the analysis of a thin-walled cylinder. For this problem, the effects of noisy strain measurements on the accuracy of the iFEM solution are examined using strain measurements that involve five and ten percent random noise, respectively. Finally, the effect of sensor locations, number of sensors, the discretization of the geometry, and the influence of noise on the strain measurements are assessed with respect to the solution accuracy.

1. Introduction

Structural health monitoring (SHM) is a procedure that obtains precise real-time information from a structure regarding its global or local structural state. The main objective of SHM is the detection of unusual structural behaviors, which pinpoint failure or an unhealthy structural condition [12]. Detection of an unhealthy condition not only contributes to the detailed inspection plan of the structure, but also reduces uncertainty concerning the structure that is being monitored. The exercise of SHM serves to both increase human and environmental safety while at the same time reducing maintenance costs. As a consequence, it is necessary to develop a SHM system that uses the measured data obtained from the on-board sensors for any type of practical engineering applications such as bridges, ships, aerospace vehicles etc.

Dynamic tracking of the three-dimensional displacement field of a structure, known as “shape sensing”, is essential to the SHM procedure. Tessler and Spangler [33] indicated that full-field structural deformations, strains and stresses can be reconstructed from the strain data obtained from a network of on-board strain sensors located at various sites of a structure. A regularization term which guarantees a confident smoothness degree to solve this inverse problem was introduced by Tikhonov and Arsenin [35] and most of the inverse methods use some type of Tikhonov’s regularization (refer to [19,21,20,24] and references therein).

Many shape sensing studies have been performed to solve the bending problem of a beam. Davis et al. [7] regenerated a simple static-beam response from a set of discrete strain data by using optimized trial functions and weights. Their approach requires many trial functions and strain sensors when more complicated deformations are predicted. Kang et al. [16] reconstructed the response of a beam, which was subjected to dynamic excitation, by using vibration mode shapes. Since their approach calculates the modal coordinates by using the strain–displacement relationship matrix and measured surface strain measurements, the number of estimated mode shapes is restricted only to the number

* Corresponding author.
E-mail addresses: adnan.kefal@strath.ac.uk (A. Kefal), erkan.oterkus@strath.ac.uk (E. Oterkus), alexander.tessler-1@nasa.gov (A. Tessler), jan.l.spangler@nasa.gov (J.L. Spangler).

Peer review under responsibility of Karabuk University.

http://dx.doi.org/10.1016/j.jestch.2016.03.006
2215-0986/

of strain sensors placed on the beam. Based on the classical beam theory, Kim and Cho [17] and Ko et al. [18] integrated discretely measured strains to calculate the continuous beam deflection. Kim and Cho [17] performed regression analysis of experimental strain data to obtain a continuous strain curvature function that leads to evaluation of the deformed shape of the beam. Ko et al. [18] computed the deflection and cross-section twist of an aircraft wing by using a load-independent method that approximates the beam curvature with piece-wise polynomials. Derkevorkian et al. [8] not only experimentally and computationally investigated the shape-estimation methodology proposed by Ko et al. [18], but also compared the methodology with the classical modal-based estimation approach. Chierichetti [5] used a numerical approach, called load confluence algorithm (LCA), to reconstruct dynamic response of two beams connected with a nonlinear spring by using the experimental measurements obtained from a few locations. However, LCA requires a numerical estimation of a loading case that corresponds to equivalent external loads applied to the system, before the regeneration of the displacement field.

In addition to the studies concerning the shape sensing of beam type structures, the real-time monitoring of plate structures has been considered by several authors. Jones et al. [15] used a least-squares formulation to solve the shape sensing problem of a cantilever honeycomb plate under arbitrary loading conditions. According to classical bending assumptions, the axial strain was fitted with a cubic polynomial and integrated with the use of approximate boundary conditions at the clamped end. Shkarayev et al. [25,26] used an inverse interpolation formulation that involves a parametric approximation of the loading and is based on a least-squares algorithm. The methodology requires the recovery of the applied loading based on spatial distribution functions, and then reconstructs the displacement field. Bogert et al. [3] discussed an inverse algorithm, which uses the deformation of the structure and strain modes together with the discrete strain data to regenerate the deformed shape of plates subjected to arbitrary static loading. Although numerically and experimentally obtained results of their plate specimen agree well, this approach requires the use of a large number of natural vibration modes. Therefore, a computationally expensive eigenvalue analysis has to be performed, especially if the method is implemented using a high-fidelity mesh. Nishio et al. [22] used a weighted-least-squares formulation to reconstruct the deflection of a composite cantilever plate from measured strain data. It is difficult to generalize their approach since the weighting coefficients in the least-square terms are computed to resolve inherent errors in the strain-sensor data by considering the given data-acquisition tool, the load condition, and the test specimen.

Most of the aforementioned inverse methods do not take into account the complexity of boundary conditions and structural topology. Moreover, they also require adequately precise loading and/or material information. Therefore, they are not powerful enough for on-board SHM procedures. A new state-of-the-art methodology named as the inverse Finite Element Method (iFEM), which satisfies the necessities of a SHM procedure, was developed by Tessler and Spangler [31,33]. The iFEM algorithm reconstructs the structural deformations from experimentally measured strains based on the minimization of a weighted-least-squares functional. Unlike the other inverse methods, the iFEM methodology is generally applicable to complex structures subjected to complicated boundary conditions in real-time [33]. The iFEM framework is precise, powerful and sufficiently fast for real-time applications of any type of static and dynamic loading, as well as a wide range of elastic materials since only the strain–displacement relationship is used in the formulation [10,11]. A U.S. patent (US 8,515,675 B2) is obtained for a system that performs shape sensing of a downhole structure by using the iFEM methodology [27].

Based on iFEM and its shape-sensing analysis capability, the structural domain can be discretized by beam, frame, plate, or shell "inverse" finite elements. The original iFEM development, by Tessler and Spangler [32], used Mindlin (first-order shear deformation) theory to develop a robust and highly efficient three-node inverse shell element (iMIN3) capable of modeling arbitrary plate and shell structures. The predictive capability of the iMIN3 element was initially assessed on numerically generated strain data, by Tessler and Spangler [32], but later was also demonstrated using experimentally measured strains, by Quach et al. [23] and Vazquez et al. [37]. Recently, Cerracchio et al. [4] and Gherlone et al. [9–11] developed a computationally efficient inverse-frame finite element based on the kinematic assumptions of Timoshenko beam theory. Their iFEM applications are tailored toward one-dimensional structures such as trusses, beams, and frames. The shape-sensing analyses of three-dimensional frame structures undergoing static or damped harmonic excitations used both numerically generated and experimentally measured strain data and showed superior predictive capabilities.

The main focus of this work is to expand the library of iFEM-based inverse shell elements, which presently includes only iMIN3, by developing a robust and computationally efficient four-node quadrilateral inverse-shell element, iQS4. This new element includes hierarchical drilling rotation degrees-of-freedom (DOF) and further extends the practical usefulness of iFEM for shape sensing analysis of large-scale structures. The iFEM formulation is based on the minimization of a weighted-least-squares functional utilizing Mindlin theory as its kinematic framework. Several validation and demonstration problems are presented. They are: (1) a cantilever rectangular plate subjected to bending force, (2) a short cantilever beam under transverse shear loading, and (3) a thin-walled cylinder. For this problem, the effects of noisy strain measurements on the accuracy of the iFEM solution are examined using strain measurements that involve five and ten percent random noise, respectively. Experimentally measured strains are simulated by strains obtained from a high-fidelity finite element solution using an in-house finite element code. In addition, several types of discretization strategies are examined and comparisons of the reconstructed iFEM and direct FEM displacement solutions are provided. By exploiting the weighting constants within the iFEM least-squares functional, it is confirmed that a relatively accurate deformed structural shape can be reconstructed in the absence of a large number of in-situ strain data. Finally, the effects of sensor locations, number of sensors, the degree of discretization refinement, and the influence of noise in the strain measurements are assessed with respect to the solution accuracy.

2. Inverse finite element formulation for shells

2.1. Quadrilateral inverse-shell element

The four-node quadrilateral inverse-shell element, labeled iQS4, is developed on the basis of a weighted-least-squares iFEM formulation, and has six displacement DOF per node (refer to Fig. 1). The beneficial aspects of this new element are such that, due to the inclusion of drilling rotations, singular solutions can be simply avoided when modeling complex shell structures and, moreover, for membrane problems, iQS4 has less tendency toward shear locking. The generic way to obtain the element formulation, writing local membrane and bending matrices for a flat geometry and adding them together, is followed because it is a satisfactory approach in terms of iFEM methodology.

The first step is to define a set of convenient coordinate frames of reference to guarantee the geometric uniqueness of the assembled shell structure. A local coordinate system (x, y, z) serves as the element frame of reference, with its origin $(0, 0, 0)$ located at

Please cite this article in press as: A. Kefal et al., A quadrilateral inverse-shell element with drilling degrees of freedom for shape sensing and structural health monitoring, Eng. Sci. Tech., Int. J. (2016), http://dx.doi.org/10.1016/j.jestch.2016.03.006

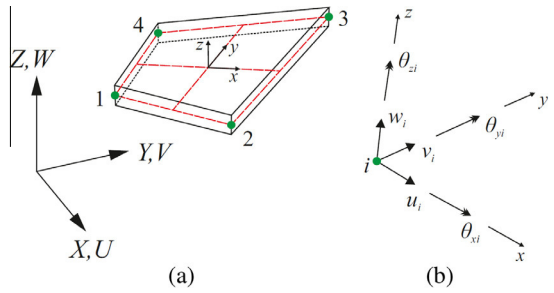

Fig. 1. (a) Four-node quadrilateral inverse-shell element, iQS4, depicted within global (X,Y,Z) and local (x,y,z) frames of reference; (b) nodal degrees-of-freedom corresponding to local (element) coordinates (x,y,z).

the centroid of the mid-plane quadrilateral. It is assumed that the shell element has a uniform thickness $2h$, and that $z \in [-h,+h]$ defines the thickness coordinate (refer to Fig. 1). With the element nodes referred to the global coordinates (X, Y, Z), suitable transformation matrices defining the local to global transformations are readily established in accordance with standard finite element procedures to assemble element matrices into a global system of equations (e.g., refer to [2]).

The (x, y) reference plane of the iQS4 quadrilateral element can be uniquely defined in terms of bilinear isoparametric shape functions $N_i(s,t)$ and the element local nodal coordinates $(x_i, y_i)\,(i = 1-4)$, where s and t are dimensionless isoparametric coordinates (refer to Fig. 2). The mapping functions can be expressed as follows:

$$x(s,t) \equiv x = \sum_{i=1}^{4} N_i x_i \tag{1a}$$

$$y(s,t) \equiv y = \sum_{i=1}^{4} N_i y_i \tag{1b}$$

where the N_i shape functions are summarized in Appendix A. The nodal DOF, consisting of positive x translations u_i, positive y translations v_i, and positive clockwise drilling rotations θ_{zi}, define the u and v membrane displacements by

$$u(x,y) \equiv u = \sum_{i=1}^{4} N_i u_i + \sum_{i=1}^{4} L_i \theta_{zi} \tag{2a}$$

$$v(x,y) \equiv v = \sum_{i=1}^{4} N_i v_i + \sum_{i=1}^{4} M_i \theta_{zi} \tag{2b}$$

where L_i and M_i are the shape functions that define the interaction between the hierarchical drilling rotation DOF and the membrane displacements of the element. These shape functions have been

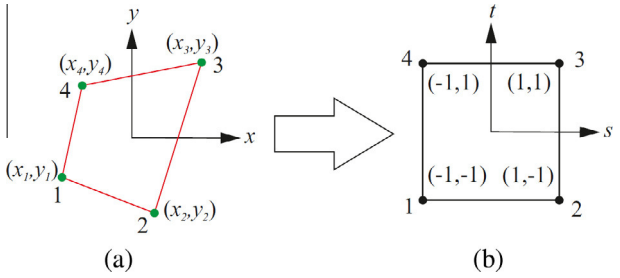

Fig. 2. (a) Mid-plane (x,y)-reference surface and nodal coordinates of iQS4 element; (b) parent element in isoparametric coordinates.

previously discussed by Cook [6]; their explicit forms are given in Appendix A.

The transverse displacement and two bending rotations w, θ_x, and θ_y are defined by the DOF of positive z translation w_i and positive counter clockwise rotations around the x- and y-axes, θ_{xi} and θ_{yi}. These kinematic variables are interpolated using the anisoparametric shape functions developed by Tessler and Hughes [28] for a four-node quadrilateral plate element, MIN4 (Mindlin-type, four-nodes). These interpolations are given as

$$w(x,y) \equiv w = \sum_{i=1}^{4} N_i w_i - \sum_{i=1}^{4} L_i \theta_{xi} - \sum_{i=1}^{4} M_i \theta_{yi} \tag{3a}$$

$$\theta_x(x,y) \equiv \theta_x = \sum_{i=1}^{4} N_i \theta_{xi} \tag{3b}$$

$$\theta_y(x,y) \equiv \theta_y = \sum_{i=1}^{4} N_i \theta_{yi} \tag{3c}$$

Utilizing Eqs. (2) and (3), the three components of the displacement vector of any material point within the element can be described as:

$$u_x(x,y,z) \equiv u_x = u + z\theta_y \tag{4a}$$

$$u_y(x,y,z) \equiv u_y = v - z\theta_x \tag{4b}$$

$$u_z(x,y,z) \equiv u_z = w \tag{4c}$$

where u_x and u_y are the in-plane displacements and u_z is the transverse displacement (deflection) across the uniform shell thickness.

The linear strain–displacement relations of linear elasticity theory are given as

$$\varepsilon_{xx} = \frac{\partial u_x}{\partial x} = \frac{\partial u}{\partial x} + z\frac{\partial \theta_y}{\partial x} \tag{5a}$$

$$\varepsilon_{yy} = \frac{\partial u_y}{\partial y} = \frac{\partial v}{\partial y} - z\frac{\partial \theta_x}{\partial y} \tag{5b}$$

$$\gamma_{xy} = \frac{\partial u_y}{\partial x} + \frac{\partial u_x}{\partial y} = \frac{\partial v}{\partial x} + \frac{\partial u}{\partial y} + z\left(\frac{\partial \theta_y}{\partial y} - \frac{\partial \theta_x}{\partial x}\right) \tag{5c}$$

$$\gamma_{xz} = \frac{\partial u_z}{\partial x} + \frac{\partial u_x}{\partial z} = \frac{\partial w}{\partial x} + \theta_y \tag{5d}$$

$$\gamma_{yz} = \frac{\partial u_z}{\partial y} + \frac{\partial u_y}{\partial z} = \frac{\partial w}{\partial y} - \theta_x \tag{5e}$$

Note that the plane-stress assumption $\sigma_{zz} = 0$ within the theory implies that the transverse-normal strain ε_{zz} does not contribute to the strain energy.

Introducing Eqs. (3) into Eqs. (5) results in the strain–displacement relations expressed in terms of the element nodal displacement vector, $\mathbf{u}^e$, as

$$\begin{Bmatrix} \varepsilon_{xx} \\ \varepsilon_{yy} \\ \gamma_{xy} \end{Bmatrix} \equiv \mathbf{e}(\mathbf{u}^e) + z\mathbf{k}(\mathbf{u}^e) = \mathbf{B}^m\mathbf{u}^e + z\mathbf{B}^b\mathbf{u}^e \tag{6a}$$

$$\begin{Bmatrix} \gamma_{xz} \\ \gamma_{yz} \end{Bmatrix} \equiv \mathbf{g}(\mathbf{u}^e) = \mathbf{B}^s\mathbf{u}^e \tag{6b}$$

where

$$\mathbf{u}^e = [\,\mathbf{u}_1^e \quad \mathbf{u}_2^e \quad \mathbf{u}_3^e \quad \mathbf{u}_4^e\,]^T \tag{6c}$$

$$\mathbf{u}_i^e = [\,u_i \quad v_i \quad w_i \quad \theta_{xi} \quad \theta_{yi} \quad \theta_{zi}\,]^T \quad (i=1,2,3,4) \tag{6d}$$

and where the matrices $\mathbf{B}^m$, $\mathbf{B}^b$, and $\mathbf{B}^s$ contain derivatives of the shape functions (refer to Appendix B).

Since the membrane strains $\mathbf{e}(\mathbf{u}^e)$, are associated with the stretching of the middle surface, the $\mathbf{B}^m$ matrix contains the derivatives of the shape functions that are associated with the membrane behavior. Moreover, the bending curvatures and transverse shear strains are represented as $\mathbf{k}(\mathbf{u}^e)$ and $\mathbf{g}(\mathbf{u}^e)$, respectively. Accordingly, the $\mathbf{B}^b$ and $\mathbf{B}^s$ matrices contain the corresponding derivatives of the shape functions that define the element bending response. The expressions for $\mathbf{B}^m$, $\mathbf{B}^b$, and $\mathbf{B}^s$ are summarized in Appendix B.

2.2. Input data from in-situ strain sensors

Discrete in-situ strain measures that are obtained from on-board sensors are crucial according to the iFEM formulation. Conventional strain rosettes or embedded fiber-optic sensor networks such as fiber Bragg grating (FBG) sensors can be used to collect a large amount of on-board strain data. In order to compute the reference plane strains and curvatures, the necessary orientation of the in-situ strain rosettes on the surface of iQS4 elements is illustrated in Fig. 3.

The experimentally measured (in-situ) membrane section strains $\mathbf{e}_i^\varepsilon$ and curvatures $\mathbf{k}_i^\varepsilon$ that correspond to their analytic counterparts, $\mathbf{e}(\mathbf{u}^e)$ and $\mathbf{k}(\mathbf{u}^e)$ given by Eq. (6), can be determined from the measured surface strains at n discrete locations $(\mathbf{x}_i = x_i, y_i, \pm h)$ $(i=1,\ldots,n)$ located within the element. These in-situ section strains are computed as follows [33]

$$\mathbf{e}_i^\varepsilon = \frac{1}{2}\begin{Bmatrix} \varepsilon_{xx}^+ + \varepsilon_{xx}^- \\ \varepsilon_{yy}^+ + \varepsilon_{yy}^- \\ \gamma_{xy}^+ + \gamma_{xy}^- \end{Bmatrix}_i \quad (i=1,n) \tag{7a}$$

and

$$\mathbf{k}_i^\varepsilon = \frac{1}{2h}\begin{Bmatrix} \varepsilon_{xx}^+ - \varepsilon_{xx}^- \\ \varepsilon_{yy}^+ - \varepsilon_{yy}^- \\ \gamma_{xy}^+ - \gamma_{xy}^- \end{Bmatrix}_i \quad (i=1,n) \tag{7b}$$

where the measured surface strains are denoted by $(\varepsilon_{xx}^+, \varepsilon_{yy}^+, \gamma_{xy}^+)_i$ and $(\varepsilon_{xx}^-, \varepsilon_{yy}^-, \gamma_{xy}^-)_i$, with the superscripts '+' and '−' denoting the quantities that correspond to the top and bottom surface locations, respectively.

Although the experimentally measured surface strains can be used to compute the in-situ membrane strains $\mathbf{e}_i^\varepsilon$ and bending curvatures $\mathbf{k}_i^\varepsilon$, they cannot be directly used to calculate the in-situ transverse shear strains $\mathbf{g}_i^\varepsilon$. A smoothing procedure, called the Smoothing Element Analysis [29,30], enables the first-order derivatives of $\mathbf{k}_i^\varepsilon$ to be accurately computed and subsequently used to obtain the transverse shear strains $\mathbf{g}_i^\varepsilon$. It is noted, however, that in the deformation of thin shells, the contributions of $\mathbf{g}_i^\varepsilon$ are much smaller compared to the bending curvatures $\mathbf{k}_i^\varepsilon$. Since most of the practical engineering applications are generally suitable to be modeled by using thin shells, the $\mathbf{g}_i^\varepsilon$ contributions can be safely omitted in the iFEM formulation.

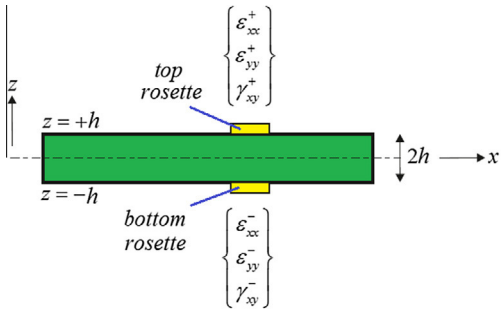

Fig. 3. Discrete surface strains measured by strain rosettes within iQS4 element at $\mathbf{x}_i = (x_i, y_i, \pm h)$ locations.

2.3. Weighted least-squares functional of inverse Finite Element Method

The already defined iFEM reconstructs the deformed shape of a discretized structure by minimizing a weighted least-squares functional with respect to the nodal DOF of the entire discretization. For an individual inverse element, this functional, $\Phi_e(\mathbf{u}^e)$, accounts for the membrane, bending and transverse shear deformations and is expressed according to [34] by

$$\Phi_e(\mathbf{u}^e) = w_e\|\mathbf{e}(\mathbf{u}^e) - \mathbf{e}^\varepsilon\|^2 + w_k\|\mathbf{k}(\mathbf{u}^e) - \mathbf{k}^\varepsilon\|^2 + w_g\|\mathbf{g}(\mathbf{u}^e) - \mathbf{g}^\varepsilon\|^2 \tag{8a}$$

The squared norms expressed in Eq. (8a) can be written in the form of the normalized Euclidean norms

$$\|\mathbf{e}(\mathbf{u}^e) - \mathbf{e}^\varepsilon\|^2 = \frac{1}{n}\int\int_{A^e}\sum_{i=1}^{n}\left(\mathbf{e}(\mathbf{u}^e)_i - \mathbf{e}_i^\varepsilon\right)^2 dxdy \tag{8b}$$

$$\|\mathbf{k}(\mathbf{u}^e) - \mathbf{k}^\varepsilon\|^2 = \frac{(2h)^2}{n}\int\int_{A^e}\sum_{i=1}^{n}\left(\mathbf{k}(\mathbf{u}^e)_i - \mathbf{k}_i^\varepsilon\right)^2 dxdy \tag{8c}$$

$$\|\mathbf{g}(\mathbf{u}^e) - \mathbf{g}^\varepsilon\|^2 = \frac{1}{n}\int\int_{A^e}\sum_{i=1}^{n}\left(\mathbf{g}(\mathbf{u}^e)_i - \mathbf{g}_i^\varepsilon\right)^2 dxdy \tag{8d}$$

where A^e represents the mid-plane area of the element. The weighting constants w_e, w_k, and w_g in Eq. (8a) are positive valued and are associated with the individual section strains. They control the complete coherence between the analytic section strains and their experimentally measured values. Their proper usage is especially critical for the problems involving relatively few locations of strain gages. When every analytic section strain has a corresponding measured in-situ value ($\mathbf{e}_i^\varepsilon$, $\mathbf{k}_i^\varepsilon$, and $\mathbf{g}_i^\varepsilon$), the weighting constants are set as $w_e = w_k = w_g = 1$ in Eqs. (8b–d).

In the case of a missing in-situ strain component, the corresponding weighting constant is set to be small, e.g., $\alpha = 10^{-4}$, and Eqs. (8b–d) take on the reduced form

$$\|\mathbf{e}(\mathbf{u}^e)\|^2 = \int\int_{A^e}\mathbf{e}(\mathbf{u}^e)^2 dxdy \text{ with } (w_e = \alpha) \tag{9a}$$

$$\|\mathbf{k}(\mathbf{u}^e)\|^2 = (2h)^2\int\int_{A^e}\mathbf{k}(\mathbf{u}^e)^2 dxdy \text{ with } (w_k = \alpha) \tag{9b}$$

$$\|\mathbf{g}(\mathbf{u}^e)\|^2 = \int\int_{A^e}\mathbf{g}(\mathbf{u}^e)^2 dxdy \text{ with } (w_g = \alpha) \tag{9c}$$

where implementation of Eqs. (9) is performed on the component-by-component basis.

Furthermore, iFEM also permits the use of 'strain-less" inverse elements – the type of elements that do not have any in-situ section-strain measurements. For these 'strain-less" elements, all squared norms in Eqs. (9) are multiplied by the small weighting constants $w_e = w_k = w_g = \alpha = 10^{-4}$. Therefore, an iFEM discretization can have very sparse measured strain data, and yet the necessary interpolation connectivity can still be maintained between the elements that have strain-sensor data.

Please cite this article in press as: A. Kefal et al., A quadrilateral inverse-shell element with drilling degrees of freedom for shape sensing and structural health monitoring, Eng. Sci. Tech., Int. J. (2016), http://dx.doi.org/10.1016/j.jestch.2016.03.006

By virtue of these assumptions, all strain compatibility relations are explicitly satisfied so that Eq. (8a) can be minimized with respect to the nodal displacement DOF, giving rise to

$$\frac{\partial \Phi_e(\mathbf{u}^e)}{\partial \mathbf{u}^e} = \mathbf{k}^e\mathbf{u}^e - \mathbf{f}^e = 0 \tag{10a}$$

or simply

$$\mathbf{k}^e\mathbf{u}^e = \mathbf{f}^e \tag{10b}$$

where $\mathbf{k}^e$ is the element left-hand-side matrix, $\mathbf{f}^e$ is the element right-hand-side vector that is a function of the measured strain values, and $\mathbf{u}^e$ is the nodal displacement vector of the element.

The element $\mathbf{k}^e$ matrix can be explicitly written in terms of the $\mathbf{B}^m$, $\mathbf{B}^b$, and $\mathbf{B}^s$ matrices and their corresponding weighting constants w_e, w_k, and w_g, and is given by

$$\mathbf{k}^e = \int\int_{A^e} (w_e(\mathbf{B}^m)^T\mathbf{B}^m + w_k(2h)^2(\mathbf{B}^b)^T\mathbf{B}^b + w_g(\mathbf{B}^s)^T\mathbf{B}^s)dxdy \tag{10c}$$

The $\mathbf{f}^e$ vector is a function of the number of strain sensors within the element as well as the measured section-strain values, and is given by

$$\mathbf{f}^e = \frac{1}{n}\int\int_{A^e}\sum_{i=1}^{n}(w_e(\mathbf{B}^m)^T\mathbf{e}_i^{\varepsilon} + w_k(2h)^2(\mathbf{B}^b)^T\mathbf{k}_i^{\varepsilon} + w_g(\mathbf{B}^s)^T\mathbf{g}_i^{\varepsilon})dxdy \tag{10d}$$

Once the element (local) matrix equations are established, the element contributions to the global linear equation system of the discretized structure can be performed as

$$\mathbf{K} = \sum_{e=1}^{nel}(\mathbf{T}^e)^T\mathbf{k}^e\mathbf{T}^e \tag{11a}$$

$$\mathbf{F} = \sum_{e=1}^{nel}(\mathbf{T}^e)^T\mathbf{f}^e \tag{11b}$$

$$\mathbf{U} = \sum_{e=1}^{nel}(\mathbf{T}^e)^T\mathbf{u}^e \tag{11c}$$

$$\mathbf{KU} = \mathbf{F} \tag{11d}$$

where $\mathbf{T}^e$ is the transformation matrix of the nodal DOF of an element from the local to the global coordinate system, $\mathbf{K}$ is the global left-hand-side matrix (symmetric matrix and independent of the measured strain values), $\mathbf{U}$ is the global nodal displacement vector, $\mathbf{F}$ is the global right-hand-side vector (function of the measured strain values), and the parameter *nel* stands for the total number of inverse finite elements.

The global left-hand-side matrix $\mathbf{K}$ includes the rigid body motion mode of the discretized structure. Therefore, it is a singular matrix. By prescribing problem-specific displacement boundary conditions, the resulting system of equations can be reduced from Eq. (11d) as

$$\mathbf{K}_R\mathbf{U}_R = \mathbf{F}_R \tag{12}$$

where $\mathbf{K}_R$ is a positive definite matrix (always non-singular), and thus it is invertible. The solution of Eq. (12a) is very fast because the matrix $\mathbf{K}_R$ remains unchanged for a given distribution of strain sensors and its inverse should be calculated only once during the length of the monitoring process. However, the right-hand-side vector $\mathbf{F}_R$ is dependent on the discrete surface strain data obtained from in-situ strain sensors. Hence, it needs to be updated during any deformation cycle. Finally, the matrix–vector multiplication $\mathbf{K}_R^{-1}\mathbf{F}_R$ gives rise to the unknown DOF vector $\mathbf{U}_R$, which provides the deformed structural shape at any real-time. By using the evaluated displacement values, the continuous strain field throughout the structure can be obtained. Furthermore, the constitutive relationship between stress and strain will allow determination of stress distribution. Finally, a suitable failure criterion can be used for damage detection as part of the SHM process.

3. Numerical examples

3.1. A cantilever plate under static transverse force near free tip

A rectangular cantilever plate subject to a static transverse force applied near the free tip has a length of 0.254 m, a height of 0.0762 m, and a uniform thickness of 3.175 mm (refer to Fig. 4). The plate is made of aluminum having an elastic modulus of 73.084 GPa and a Poisson's ratio of 0.33. The concentrated force of $F = 25.728$ N is applied in the negative z direction near the tip. This plate was originally analyzed and then tested in a mechanics laboratory by Bogert et al. [3]. Subsequently, Tessler and Spangler [32] analyzed this plate configuration using the iFEM methodology. Using a relatively coarse iMIN3 discretization that has a single strain rosette within each element, the authors obtained a highly accurate reconstruction of the full-field displacement response.

In this first example, the above stated problem is analyzed once again using the iFEM/iQS4 methodology to validate the present element bending capability. There is no need to model the part of the plate to the right of the applied force because it is free of stress. Therefore, the following iFEM and direct finite element method (FEM) models are defined over the domain $X \in [0, a]$ and $Y \in [0, b]$ (refer to Figs. 4 and 5). To establish an accurate reference solution, a convergence study was performed using direct FEM analyses utilizing an in-house FEM code. The most refined mesh consisted of 432 uniformly distributed square elements, possessing 2886 DOF. The FEM deflections and rotations are used to compute the simulated strain-sensor strains.

To remain consistent with the work by Tessler and Spangler [32], in the present iFEM analysis the same strain-rosette locations are used. As depicted in Fig. 5, the iQS4 model has 28 rectangular-shaped elements each having a single strain rosette. Except for eight of the strain-rosettes (i.e., the first four which are near to the clamped edge and the second four which are near to the loading edge), the strain rosettes are placed at the centroids of each iQS4 element. Since the material properties of the plate are symmetric with respect to the mid-plane and the resulting deformations are due to bending only, the strain distribution is anti-symmetric with respect to the mid-plane and hence the strain rosettes need only be positioned on one of the bounding surfaces (in this case, the top surface) of the iQS4 elements.

In Figs. 6–8, contour plots for the transverse displacement and two bending rotations are compared between the iFEM and high-fidelity FEM analyses. The percent difference between the iFEM and FEM predictions for the maximum deflection is only 0.4%; this result is in close agreement with the predictions of Tessler and Spangler [32]. Similar accuracy is evidenced for the maximum bending rotations, with the percent difference of 0.3% for the Y-rotation, and 1.5% for the X-rotation. Both the iFEM and direct FEM contours are graphically indistinguishable in the figures. These results also confirm the superior bending predictions of iQS4, especially considering the low-fidelity mesh used in the iFEM analysis.

3.2. A short cantilever beam under shear loading

The shear-loaded short cantilever beam has been used by many authors, e.g., Allman [1], Ibrahimbegovic et al. [13] and

Please cite this article in press as: A. Kefal et al., A quadrilateral inverse-shell element with drilling degrees of freedom for shape sensing and structural health monitoring, Eng. Sci. Tech., Int. J. (2016), http://dx.doi.org/10.1016/j.jestch.2016.03.006

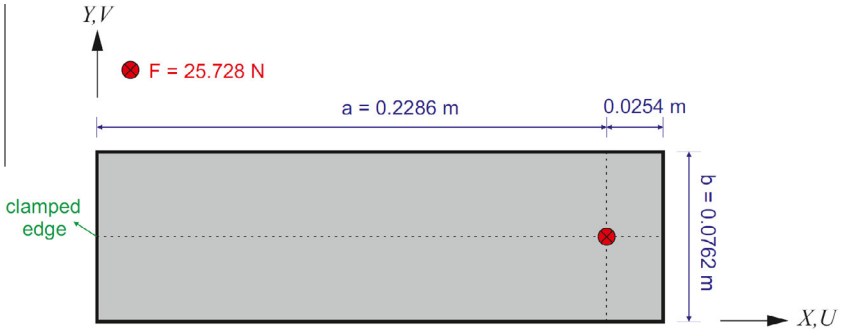

Fig. 4. Cantilever plate under transverse force applied near free tip.

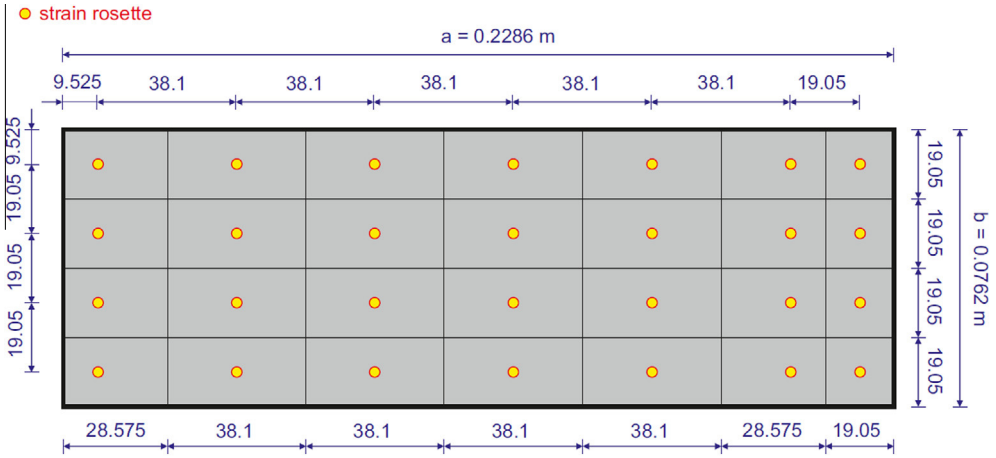

Fig. 5. Plate discretization using 28 iQS4 elements and exact locations [mm] of strain rosettes.

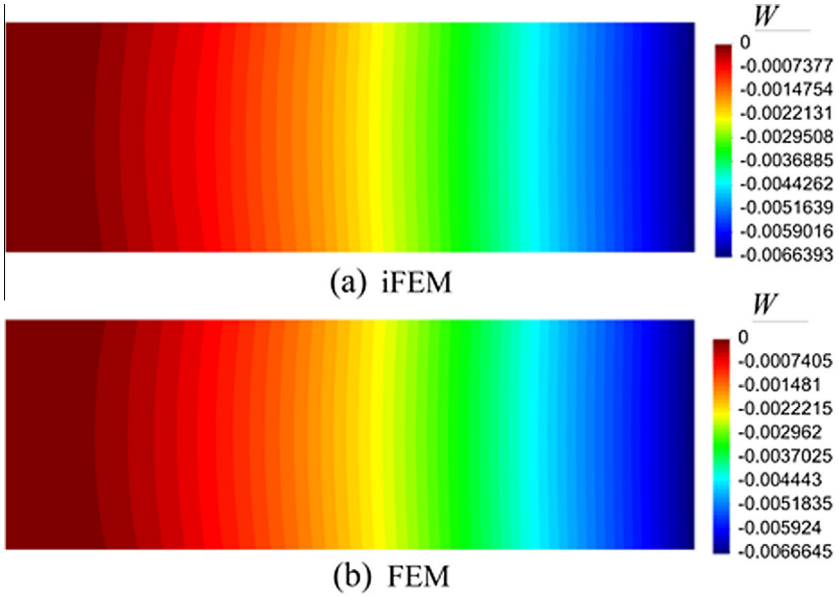

Fig. 6. Contour plots of W displacement: (a) iFEM analysis using 28 iQS4 elements and a single strain rosette per element; (b) direct FEM analysis.

Ibrahimbegovic and Wilson [14], to validate the membrane response of new elements. Herein this problem is revisited to assess the membrane capability of iQS4. The length L, the dimensions $a \times 2h$ of the constant rectangular cross section, the elastic modulus E, and the Poisson's ratio v of the beam are given in Fig. 9. The right edge of the beam is subjected to a shear loading P, whereas the left edge of the beam is fully clamped.

According to Timoshenko and Goodier [36], the elasticity solution of the V displacement of the tip is $V = \frac{2PL^3}{Eha^3} + \frac{(4+5v)PL}{4Eah} = 9.025$ mm for the properties described in

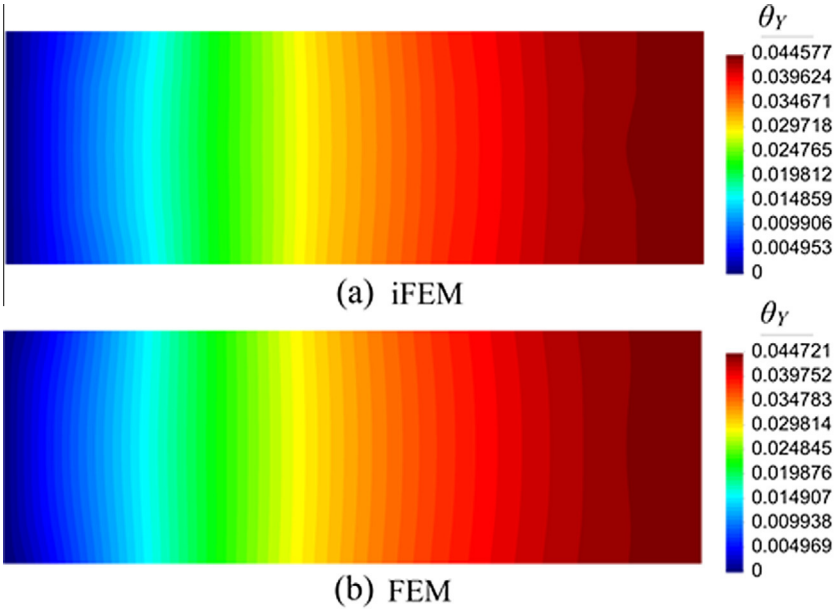

Fig. 7. Contour plots of θ_Y rotation: (a) iFEM analysis using 28 iQS4 elements and a single strain rosette per element; (b) direct FEM analysis.

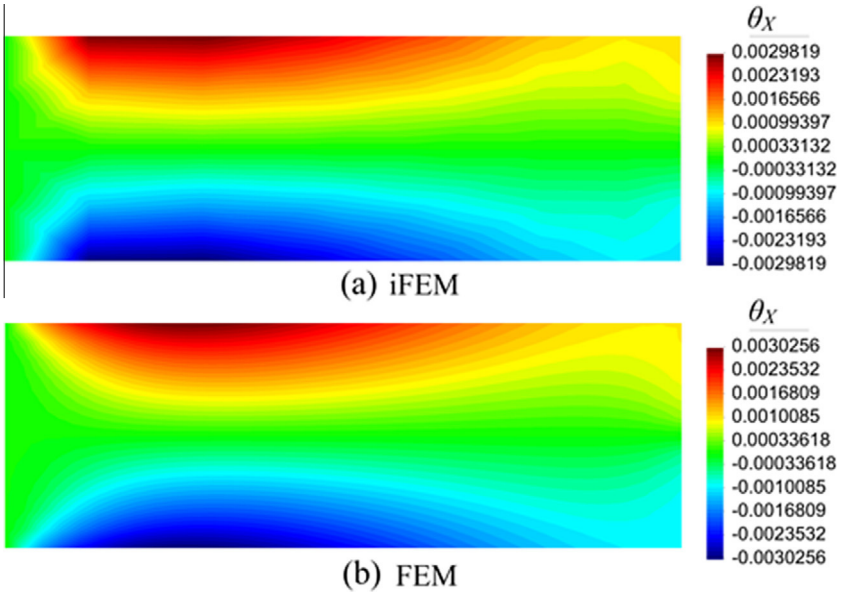

Fig. 8. Contour plots of θ_X rotation: (a) iFEM analysis using 28 iQS4 elements and a single strain rosette per element; (b) direct FEM analysis.

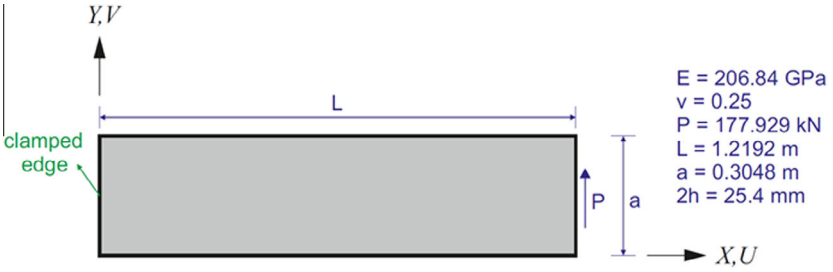

Fig. 9. Short cantilever beam under shear loading at free edge.

Please cite this article in press as: A. Kefal et al., A quadrilateral inverse-shell element with drilling degrees of freedom for shape sensing and structural health monitoring, Eng. Sci. Tech., Int. J. (2016), http://dx.doi.org/10.1016/j.jestch.2016.03.006

Fig. 9. To establish an accurate reference solution, a convergence study was performed using direct FEM analysis. The highest fidelity mesh has 1024 uniformly distributed square elements and 2210 DOF. The maximum V displacement obtained from the direct FEM analysis is approximately 9.042 mm which agrees well with the analytical solution. These FEM deflections are used to calculate the simulated in-situ strains.

Two different iFEM beam analyses are performed using varying number of strain rosettes. Since the material properties and the resulting membrane deformations of the beam are symmetric with respect to the mid-plane, the strain rosettes can be placed on one of the bounding surfaces (in this case, the top surface). In the first example, the iQS4 model of the beam has 64 square-shaped elements each having a single rosette as depicted in Fig. 10.

To investigate the effect of drilling rotation, the iFEM beam analyses are performed by both including and excluding the drilling rotation. In Fig. 11, contour plots for the V displacements are compared between these two cases. The iFEM and direct FEM analyses produce the maximum V displacement that differs only by 0.5% when the drilling rotation is included; it is 6.2% when the drilling rotation is excluded.

In the second example, the same problem is analyzed once again using a coarser iQS4 discretization that has only 16 square-shaped elements, each having a single-strain rosette as illustrated in Fig. 12. To demonstrate the effect of drilling rotation on the membrane response, contour plots of the V displacement are shown in Fig. 13, where the results correspond to the cases of including and excluding the drilling rotation. The iFEM and direct FEM predictions for the maximum deflection are identical when the drilling rotation is included in the iQS4 element formulation. By excluding the drilling rotation, the maximum V displacement is underestimated by 19.2%. These results demonstrate that iQS4 has a superior membrane-response capability when implemented with the hierarchical drilling rotation. The formulation also decreases the tendency toward membrane locking.

3.3. A thin-walled cylinder

In the previous examples, bending and membrane capabilities of the iQS4 element have been assessed by way of simple plate and beam problems. In many practical engineering applications, however, more complicated structural topologies are common. Herein, a thin-walled cylinder having radius of 1 m, length of 5 m and uniform thickness of 20 mm is analyzed to demonstrate the robustness of the iFEM/iQS4 methodology for modeling realistic shell structures. The cylinder is made of steel having an elastic modulus of 210 GPa and the Poisson's ratio of 0.3. Both ends of the cylinder are fixed in terms of translations and rotations and a concentrated force $F = 100$ kN is applied at twelve different locations (refer to Fig. 14).

The prescribed boundary conditions and geometry are suitable to take advantage of the symmetry planes. As shown in Fig. 15, only one-eighth of the cylinder needs to be modeled while applying the appropriate symmetry boundary conditions. The translations along the normal axis and the rotations around the in-plane axes are constrained for each symmetry plane. Thus, the XY-plane symmetry conditions are imposed constraining the translation along the Z-direction and the rotations around the X- and Y-directions. To establish an accurate reference solution for this problem, an FEM convergence study was carried out. The highest fidelity mesh has 2400 uniformly distributed rectangular elements and 15,006 DOF. The FEM deflections and rotations are used to calculate the simulated strain-sensor strains. Then, three different iFEM analyses of the cylinder were performed using three different strain-rosette networks. Although the material properties of the cylinder are symmetric with respect to the mid-plane, the resulting deformations exhibit both stretching and bending response due to the complexity of the structural topology. Hence, the strain-rosettes have to be placed on both the top and bottom surfaces of the cylinder.

In the first case study, the iQS4 discretization is identical to the highest-fidelity mesh used in the direct FEM analysis. As presented in Fig. 16, the iQS4 model has 2400 uniformly distributed rectangular elements each having two strain rosettes, one on the centroid of the top surface and the other one on the centroid of the bottom surface.

To assess the global displacement and rotation response, it is convenient to compute the total displacement, U_T,

$$U_T = \sqrt{U^2 + V^2 + W^2} \tag{13}$$

and the total rotation, θ_T,

$$\theta_T = \sqrt{(\theta_X)^2 + (\theta_Y)^2 + (\theta_Z)^2} \tag{14}$$

where U, V, and W are the translations along the global X-, Y-, and Z-axes, respectively, and θ_X, θ_Y, and θ_Z are the rotations around the global X-, Y-, and Z-axes, respectively.

In Figs. 17 and 18, the iFEM and FEM contour plots for U_T and θ_T are presented, showing the results that are graphically indistinguishable. The percent difference between the iFEM and FEM solutions for the maximum values of U_T and θ_T are respectively 1% and 0.06%.

Although the results of this case study are satisfactory, the number of strain rosettes used may be considered too high for a practical application. In the second case study shown in Fig. 19, the top- and bottom-surface strain-rosettes are removed from 2160 iQS4 elements, with the resulting iQS4 mesh having only 240×2 strain rosettes. For an iQS4 element which has no in-situ strain components, the corresponding weighting coefficients are set to 10^{-4}.

In Figs. 20 and 21, the contour plots for the U_T displacement and θ_T rotation are depicted for both the iFEM and high-fidelity FEM analyses. The percent difference between the iFEM and FEM predictions for the maximum U_T displacement is 3%, whereas it is only

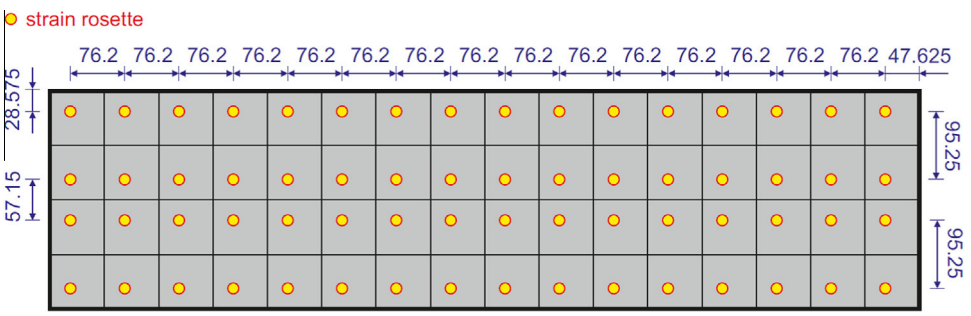

Fig. 10. Short cantilever beam discretized using 64 iQS4 elements and exact locations [mm] of strain rosettes.

Please cite this article in press as: A. Kefal et al., A quadrilateral inverse-shell element with drilling degrees of freedom for shape sensing and structural health monitoring, Eng. Sci. Tech., Int. J. (2016), http://dx.doi.org/10.1016/j.jestch.2016.03.006

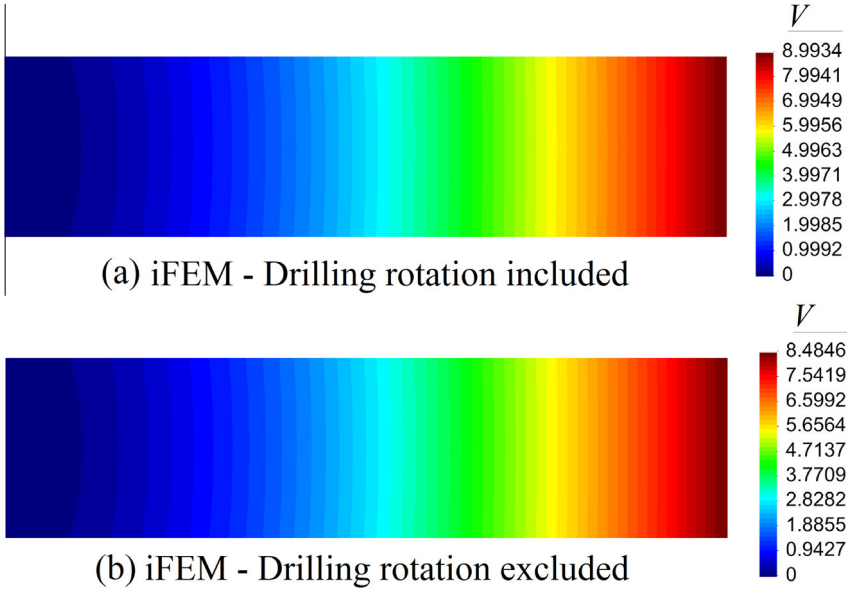

Fig. 11. Contour plots of V displacement for short cantilever beam corresponding to iFEM analysis of 64 iQS4 element model: (a) drilling rotation included; (b) drilling rotation excluded.

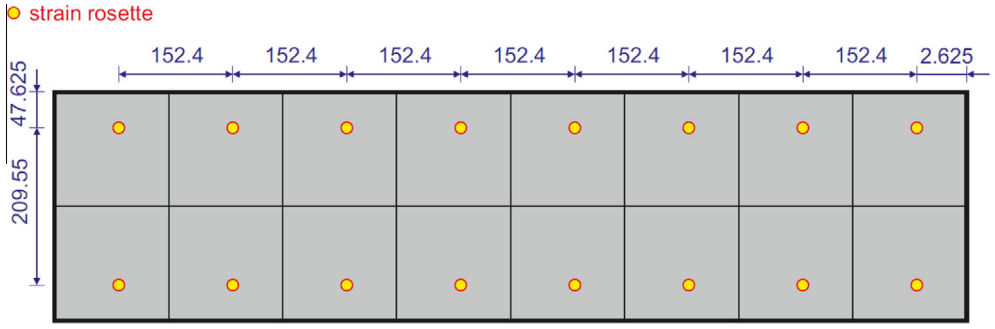

Fig. 12. Short cantilever beam discretized using 16 iQS4 elements and exact locations [mm] of strain rosettes.

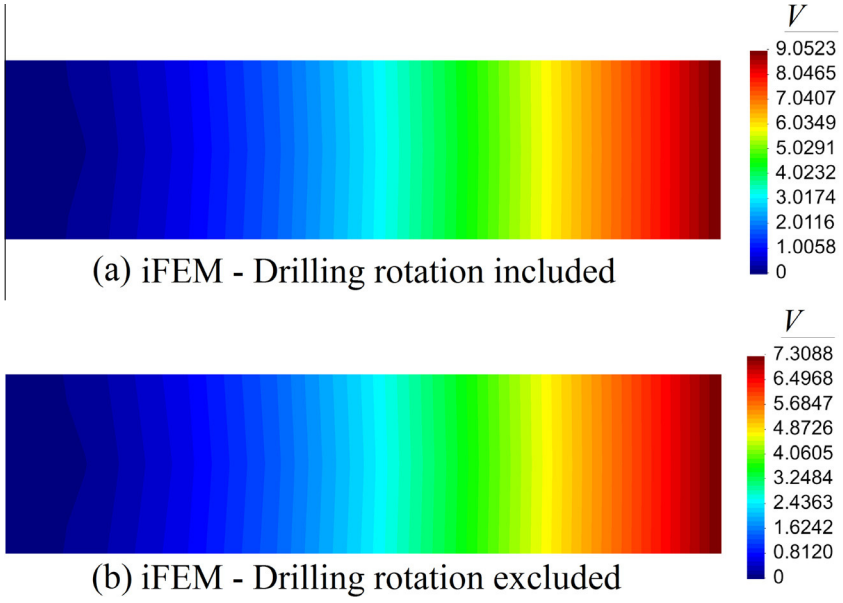

Fig. 13. Contour plots of V displacement for short cantilever beam corresponding to iFEM analysis of 16 iQS4 element model: (a) drilling rotation included; (b) drilling rotation excluded.

Please cite this article in press as: A. Kefal et al., A quadrilateral inverse-shell element with drilling degrees of freedom for shape sensing and structural health monitoring, Eng. Sci. Tech., Int. J. (2016), http://dx.doi.org/10.1016/j.jestch.2016.03.006

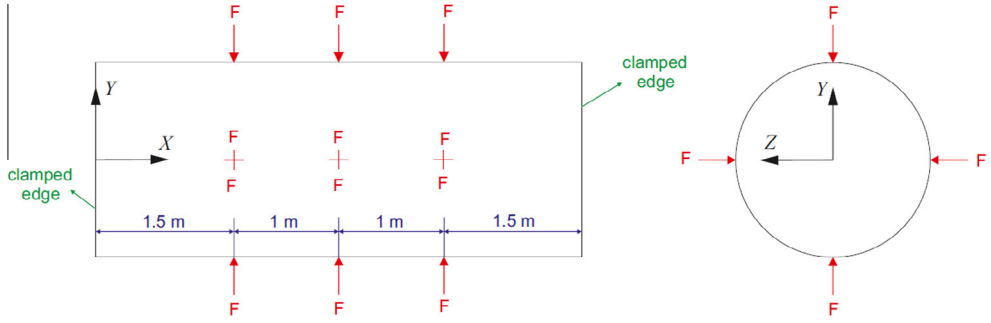

Fig. 14. Thin-walled cylinder under concentrated forces.

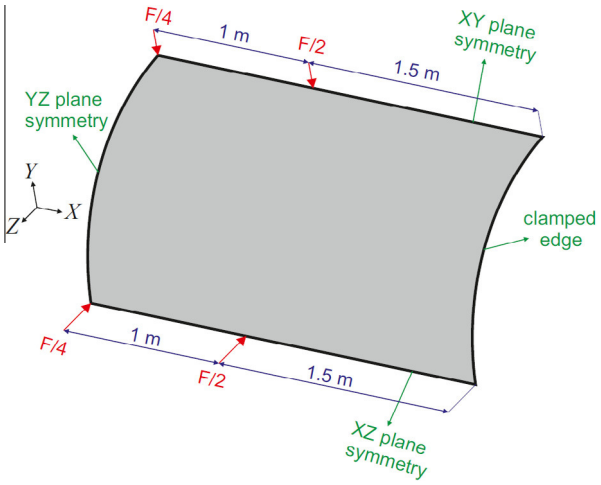

Fig. 15. One-eighth of thin-walled cylinder with symmetric boundary conditions.

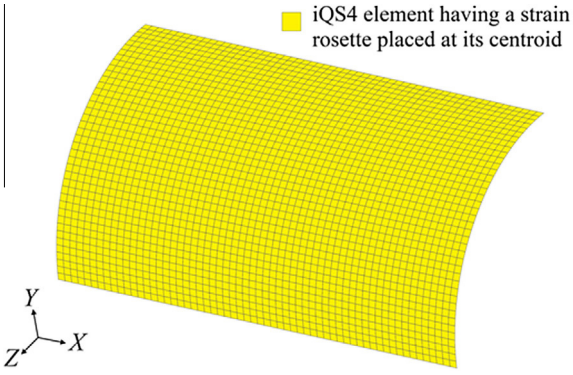

Fig. 16. Discretization of one-eighth of thin-walled cylinder using 2400 iQS4 elements with top- and bottom-surface strain rosettes per each element.

0.5% for maximum total rotation. Remarkably, the iFEM contours are almost identical to those of FEM. The iFEM predictions remain sufficiently accurate even with the missing strain-rosette data in many elements.

In the third case study, the iQS4 model of the cylinder has 160 uniformly distributed rectangular elements each having top- and bottom-surface strain rosettes located as shown in Fig. 22. The iFEM analysis is performed using the strain data obtained from 160×2 strain rosettes only.

In Figs. 23 and 24, the contour plots for the U_T displacement and θ_T rotation are presented for both the iFEM and high-fidelity FEM analyses. According to the contour plots in Fig. 23, the percent difference between the iFEM and FEM predictions for the maximum U_T displacements is less than 1%. These results demonstrate the superior accuracy of the iFEM/iQS4 capability even when very coarse discretizations are used. Even though the percent difference between the iFEM and FEM predictions for the maximum θ_T rotation is approximately 29%, the iFEM and FEM contour plots are generally in good agreement (refer to Fig. 24).

3.4. The effects of noisy strain measurements on the accuracy of the iFEM solution

The iFEM/iQS4 methodology is ultimately aimed at real engineering structures where the measured strains may be relatively noisy. Therefore, to examine iFEM/iQS4 predictive capabilities in the presence of noisy strain data, the thin-walled cylinder considered in the previous study is revisited herein. The iFEM analyses of the cylinder are performed once again using strain data which have 5% and 10% of noise, respectively.

Signal-to-noise ratio (SNR) characterizes the relative strength of a desired signal and background noise. The SNR describes the ratio of the amplitude of the signal to the amplitude of the noise. Since SNR is a dimensionless quantity and many signals can have a wide dynamic range, SNR can be expressed on the logarithmic decibel (dB) scale as

$$SNR_{\mathrm{dB}} = 10\log_{10}\left(\frac{P_{signal}}{P_{noise}}\right) \tag{15}$$

where P_{signal} and P_{noise} are respectively the average power of the signal and noise. Eq. (15) indicates that a larger SNR typically results in a less noisy measurement, whereas a smaller SNR results in a more noisy measurement.

Using Eq. (15), SNR values corresponding to 5% noise and 10% noise can be calculated as 13.01 dB and 10 dB, respectively. The white Gaussian noise is added to the surface strain measurements for each of the specified SNR values using the built-in function *awgn*() in the Matlab/Octave toolbox. In Figs. 25 and 26, the top surface strain measurements $(\varepsilon_{xx}^{+})_i$ with 0% noise are compared to those with 5% and 10% noise. These comparisons show that the added noise levels generate significant differences in the strain measurements for each sensor.

Once the iFEM analyses of the thin-walled cylinder are performed using strain data that include 5% and 10% noise levels, percent difference between iFEM and direct FEM predictions for U_T displacement can be calculated for each node i as

$$PD(U_T) = PD_i = \left|\frac{U_{T,i}^{\mathrm{iFEM}} - U_{T,i}^{\mathrm{FEM}}}{U_{T,\max}^{\mathrm{FEM}}}\right| \times 100\% \tag{16}$$

where $U_{T,i}^{\mathrm{iFEM}}$ is iFEM prediction for the U_T displacement at node i, $U_{T,i}^{\mathrm{FEM}}$ is direct FEM prediction for the U_T displacement at node i,

Please cite this article in press as: A. Kefal et al., A quadrilateral inverse-shell element with drilling degrees of freedom for shape sensing and structural health monitoring, Eng. Sci. Tech., Int. J. (2016), http://dx.doi.org/10.1016/j.jestch.2016.03.006

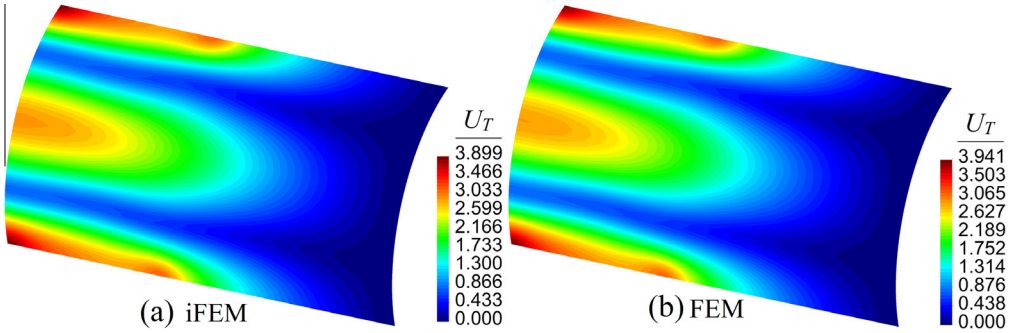

Fig. 17. Contour plots of U_T displacement for thin-walled cylinder modeled in Fig. 16: (a) iFEM/iQS4 analysis; (b) direct FEM analysis.

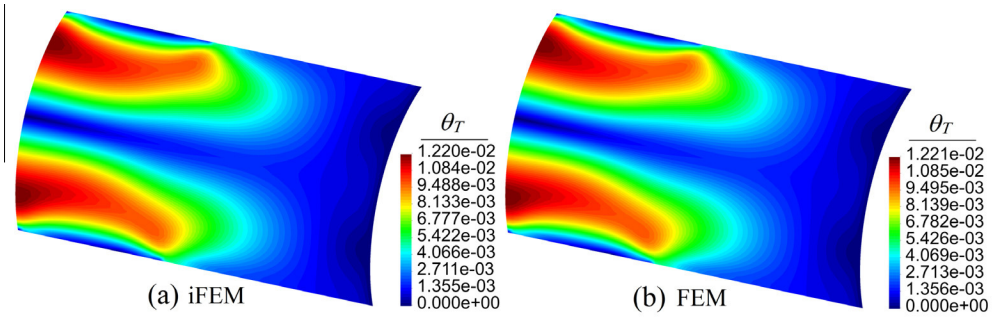

Fig. 18. Contour plots of θ_T rotation for thin-walled cylinder modeled in Fig. 16: (a) iFEM/iQS4 analysis; (b) direct FEM analysis.

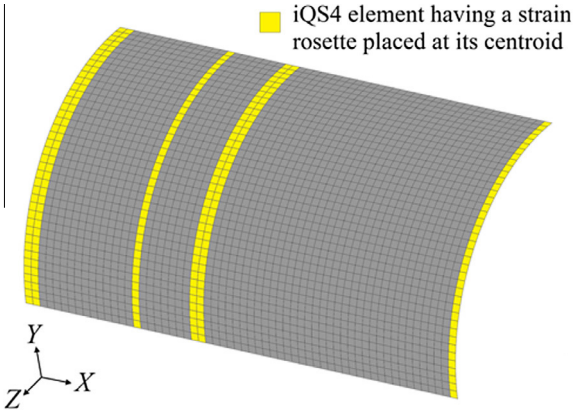

Fig. 19. Discretization of one-eighth of thin-walled cylinder using 2400 iQS4 elements with top- and bottom-surface strain rosettes located within 240 select elements.

and $U_{T,\max}^{\text{FEM}}$ is direct FEM prediction of the maximum U_T displacement. In Fig. 27, contour plots of $PD(U_T)$, corresponding to the model in Fig. 16, are shown for the strain data with the noise levels of 0%, 5%, and 10%. The results clearly demonstrate the superior accuracy of the iFEM solutions even when the in-situ strain measurements include noise up to 10%. Moreover, the mean-percent difference, MPD, and the root-mean-square difference, RMSD, comparing iFEM and FEM predictions for the U_T displacement, are calculated as

$$\text{MPD} = \frac{1}{N_n}\sum_{i=1}^{N_n} PD_i \tag{17}$$

and

$$\text{RMSD} = \sqrt{\frac{\sum_{i=1}^{N_n}\left(U_{T,i}^{\text{iFEM}} - U_{T,i}^{\text{FEM}}\right)^2}{N_n}} \tag{18}$$

where N_n is the total number of nodes. As shown in Table 1, MPD and RMSD for the U_T displacement for each iFEM/iQS4 model are

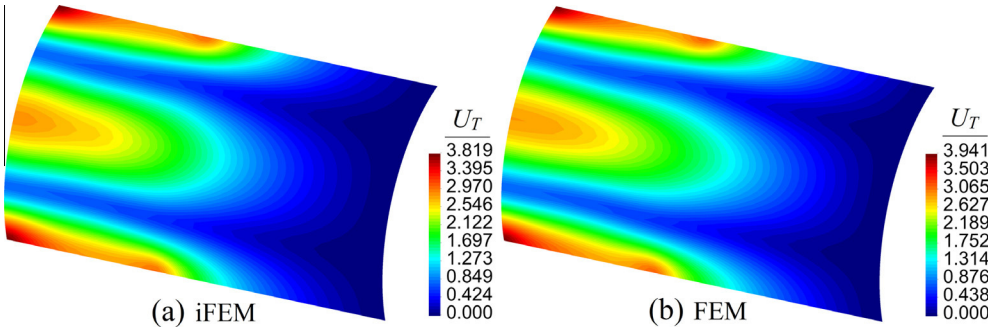

Fig. 20. Contour plots of U_T displacement for thin-walled cylinder modeled in Fig. 19: (a) iFEM/iQS4 analysis; (b) direct FEM analysis.

Please cite this article in press as: A. Kefal et al., A quadrilateral inverse-shell element with drilling degrees of freedom for shape sensing and structural health monitoring, Eng. Sci. Tech., Int. J. (2016), http://dx.doi.org/10.1016/j.jestch.2016.03.006

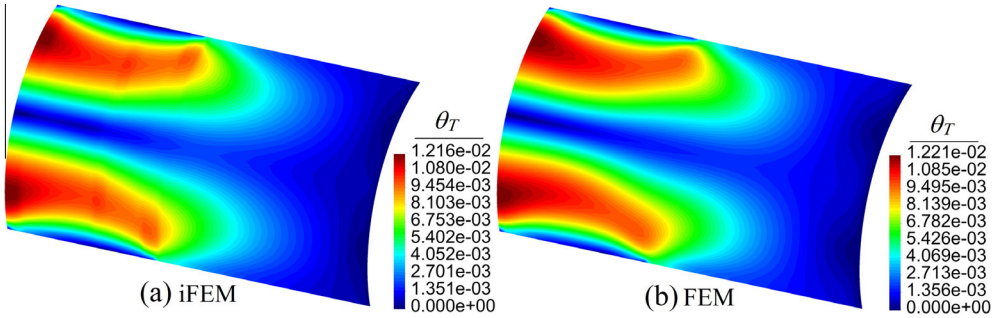

Fig. 21. Contour plots of θ_T rotation for thin-walled cylinder modeled in Fig. 19: (a) iFEM/iQS4 analysis; (b) direct FEM analysis.

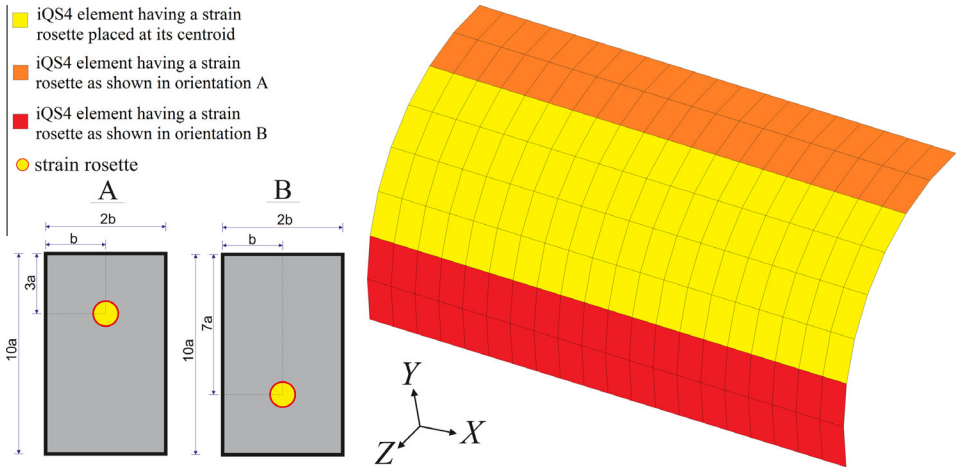

Fig. 22. Discretization of one-eighth of thin-walled cylinder using 160 iQS4 elements with top- and bottom-surface strain rosettes located within each element.

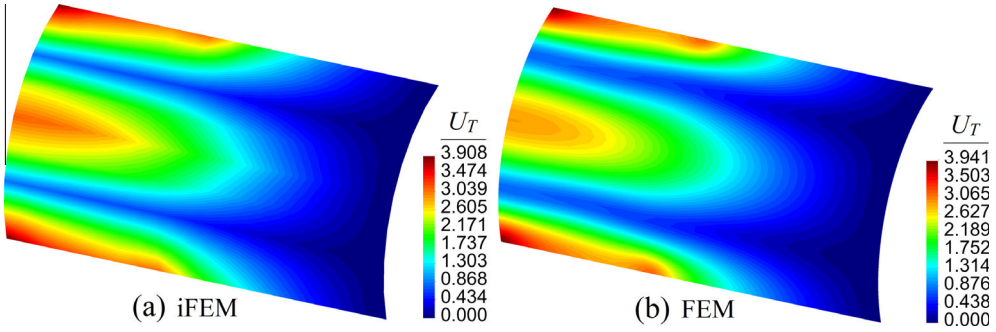

Fig. 23. Contour plots of U_T displacement for thin-walled cylinder modeled in Fig. 22: (a) iFEM/iQS4 analysis; (b) direct FEM analysis.

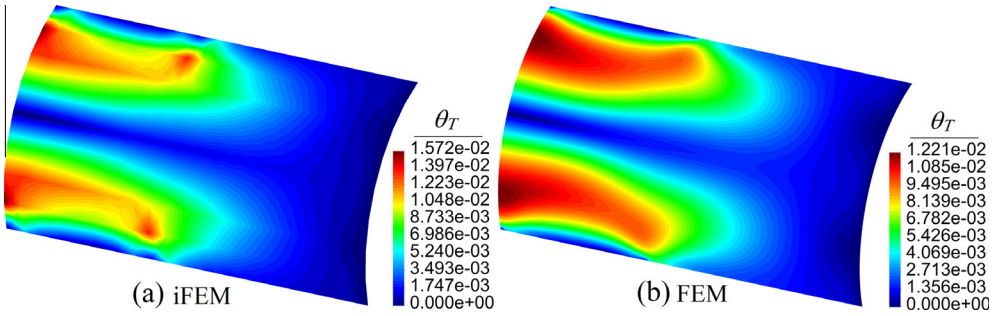

Fig. 24. Contour plots of θ_T rotation for thin-walled cylinder modeled in Fig. 22: (a) iFEM/iQS4 analysis; (b) direct FEM analysis.

Please cite this article in press as: A. Kefal et al., A quadrilateral inverse-shell element with drilling degrees of freedom for shape sensing and structural health monitoring, Eng. Sci. Tech., Int. J. (2016), http://dx.doi.org/10.1016/j.jestch.2016.03.006

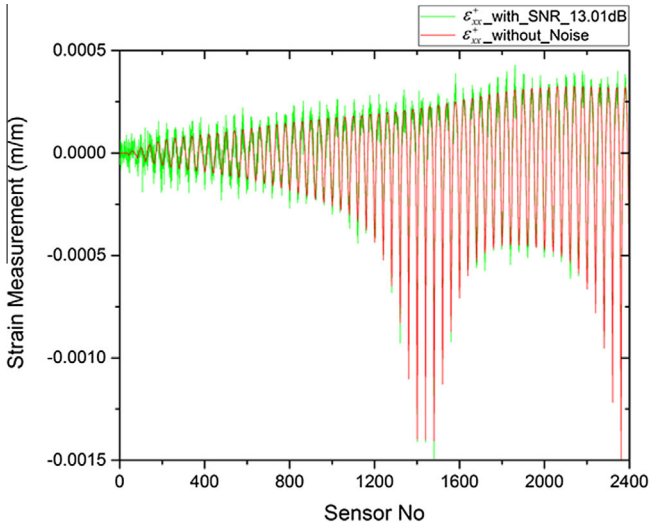

Fig. 25. Comparison of the top surface strain measurements $(\varepsilon^+_{xx})_i$ with 0% and 5% noise.

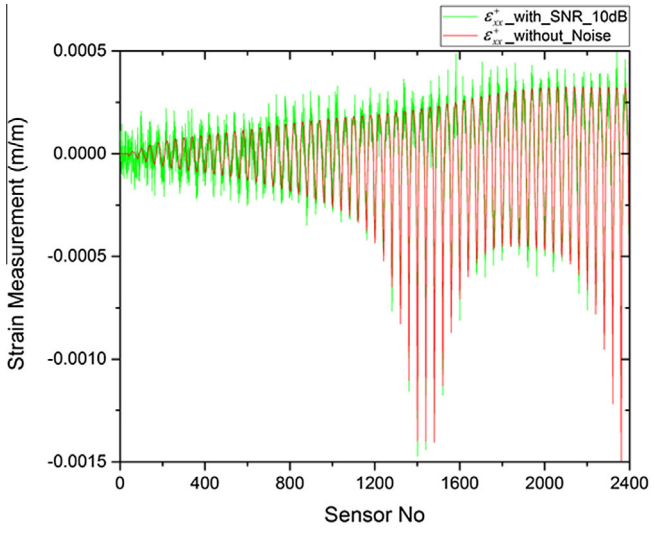

Fig. 26. Comparison of the top surface strain measurements $(\varepsilon^+_{xx})_i$ with 0% and 10% noise.

compared for the cases of 0%, 5%, and 10% noise levels for the strain measurements. The results indicate that noisy strain measurements have only insignificant effect on the accuracy of the iFEM solution.

4. Concluding remarks

A new four-node quadrilateral inverse-shell element (iQS4) has been developed for shape-sensing analysis of plate and shell structures which have randomly distributed strain sensors. The element formulation is based on a weighted least-squares variational principle originally developed by Tessler and Spangler. The element kinematic field accommodates quadratic interpolation functions that permit a robust drilling degree-of-freedom implementation that has the advantage of avoiding singular solutions when modeling complex shell structures. The formulation is also robust with respect to the membrane and shear locking phenomena. Several numerical studies have been performed and demonstrated the computational efficiency, high accuracy and robustness of iQS4 discretizations with respect to the membrane, bending, and membrane-bending coupled structural response. The practical utility of the iFEM/iQS4 technology for application to engineering structures has been assessed using relatively low- and high-fidelity discretization strategies. The effects of sensor locations, number of sensors, and inherent errors in the measured strain data have also been explored. It has been demonstrated that even in the presence of the relatively sparse strain data that are subject to experimental noise, sufficiently accurate reconstruction of the deformed structural shapes can be achieved.

Finally, the iFEM/iQS4 technology is readily implemented in any general-purpose finite element code and represents a viable computational tool for real-time structural health monitoring of general plate and shell structures.

Acknowledgement

The first author dedicates this work to a material science research pioneer, Prof. Dr. M. Cengiz Dökmeci, for filling his student's heart with the love of science.

Appendix A.

The shape functions N_i, L_i, and M_i, which are used to describe both membrane and bending capability of the iQS4 element as given in Eqs. (2a–b) and (3a–c), are respectively defined as

$$N_1 = \frac{(1-s)(1-t)}{4} \tag{A.1}$$

$$N_2 = \frac{(1+s)(1-t)}{4} \tag{A.2}$$

$$N_3 = \frac{(1+s)(1+t)}{4} \tag{A.3}$$

$$N_4 = \frac{(1-s)(1+t)}{4} \tag{A.4}$$

$$N_5 = \frac{(1-s^2)(1-t)}{16} \tag{A.5}$$

$$N_6 = \frac{(1+s)(1-t^2)}{16} \tag{A.6}$$

$$N_7 = \frac{(1-s^2)(1+t)}{16} \tag{A.7}$$

$$N_8 = \frac{(1-s)(1-t^2)}{16} \tag{A.8}$$

and

$$L_1 = y_{14}N_8 - y_{21}N_5 \tag{A.9}$$

$$L_2 = y_{21}N_5 - y_{32}N_6 \tag{A.10}$$

$$L_3 = y_{32}N_6 - y_{43}N_7 \tag{A.11}$$

$$L_4 = y_{43}N_7 - y_{14}N_8 \tag{A.12}$$

$$M_1 = x_{41}N_8 - x_{12}N_5 \tag{A.13}$$

$$M_2 = x_{12}N_5 - x_{23}N_6 \tag{A.14}$$

Please cite this article in press as: A. Kefal et al., A quadrilateral inverse-shell element with drilling degrees of freedom for shape sensing and structural health monitoring, Eng. Sci. Tech., Int. J. (2016), http://dx.doi.org/10.1016/j.jestch.2016.03.006

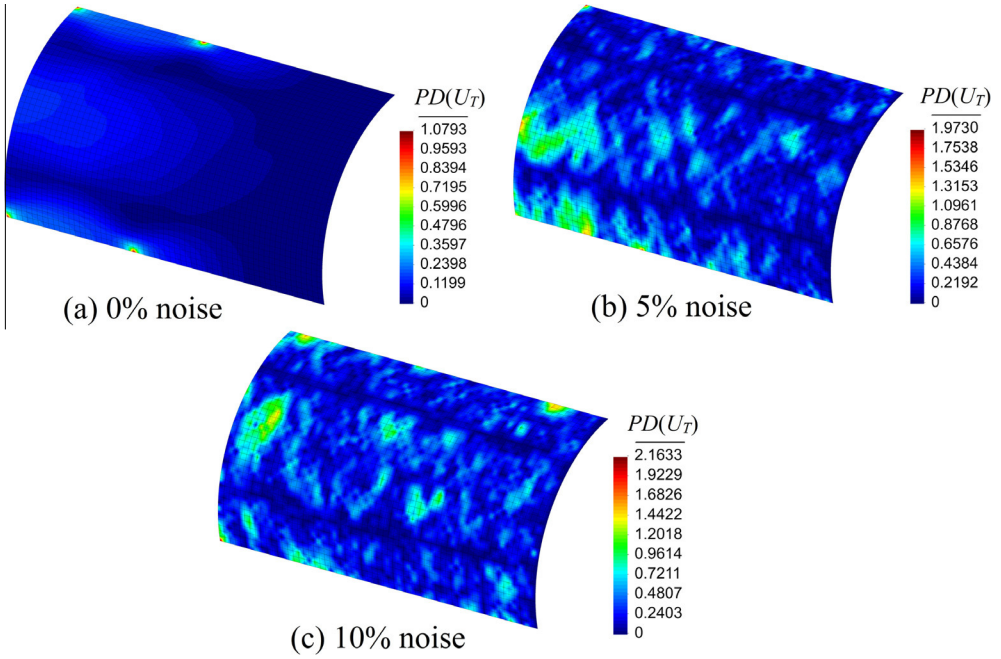

Fig. 27. Contour plots of $PD(U_T)$ for thin-walled cylinder modeled in Fig. 16, corresponding to percent noise in strain measurements: (a) 0%, (b) 5%, and (c) 10%.

Table 1
Mean-percent difference (MPD) and root-mean-square difference (RMSD) for U_T displacement corresponding to iFEM/iQS4 models with noisy strain measurements.

iFEM/iQS4 model	MPD			RMSD		
	0% noise	5% noise	10% noise	0% noise	5% noise	10% noise
1	0.0667	0.2628	0.2978	0.0040	0.0139	0.0155
2	2.0050	2.2960	2.6680	0.0954	0.1143	0.1336
3	0.7230	0.8771	0.9138	0.0379	0.0426	0.0493

$$M_3 = x_{23}N_6 - x_{34}N_7 \tag{A.15}$$

$$M_4 = x_{34}N_7 - x_{41}N_8 \tag{A.16}$$

Note that x_{ij} and y_{ij} can be expressed in terms of local coordinates of iQS4 element as

$$\left.\begin{aligned} x_{ij} &= x_i - x_j \\ y_{ij} &= y_i - y_j \end{aligned}\right\} \quad (i = 1,2,3,4;\ j = 1,2,3,4) \tag{A.17}$$

and the parent space coordinates are defined as $s, t \in [-1, +1]$.

Appendix B.

The derivatives of shape functions $\mathbf{B}^m$, $\mathbf{B}^b$, $\mathbf{B}^s$ which are given in Eqs. (6a–b) are defined as

$$\mathbf{B}^m = \begin{bmatrix} \mathbf{B}_1^m & \mathbf{B}_2^m & \mathbf{B}_3^m & \mathbf{B}_4^m \end{bmatrix} \tag{B.1}$$

$$\mathbf{B}^b = \begin{bmatrix} \mathbf{B}_1^b & \mathbf{B}_2^b & \mathbf{B}_3^b & \mathbf{B}_4^b \end{bmatrix} \tag{B.2}$$

$$\mathbf{B}^s = \begin{bmatrix} \mathbf{B}_1^s & \mathbf{B}_2^s & \mathbf{B}_3^s & \mathbf{B}_4^s \end{bmatrix} \tag{B.3}$$

where

$$\left.\begin{aligned} \mathbf{B}_i^m &= \begin{bmatrix} N_{i,x} & 0 & 0 & 0 & 0 & L_{i,x} \\ 0 & N_{i,y} & 0 & 0 & 0 & M_{i,x} \\ N_{i,y} & N_{i,x} & 0 & 0 & 0 & L_{i,y} + M_{i,x} \end{bmatrix} \\ \mathbf{B}_i^b &= \begin{bmatrix} 0 & 0 & 0 & 0 & N_{i,x} & 0 \\ 0 & 0 & 0 & -N_{i,y} & 0 & 0 \\ 0 & 0 & 0 & -N_{i,x} & N_{i,y} & 0 \end{bmatrix} \\ \mathbf{B}_i^s &= \begin{bmatrix} 0 & 0 & N_{i,x} & -L_{i,x} & -M_{i,x} + N_i & 0 \\ 0 & 0 & N_{i,y} & -L_{i,y} - N_i & -M_{i,y} & 0 \end{bmatrix} \end{aligned}\right\} \quad (i = 1,2,3,4) \tag{B.4}$$

Note that N_i, L_i, and M_i, are the shape functions of the iQS4 element which are explicitly given in Appendix A.

References

[1] D.J. Allman, A quadrilateral finite element including vertex rotations for plane elasticity analysis, Int. J. Numer. Methods Eng. 26 (3) (1988) 717–730.
[2] K.J. Bathe, Finite element procedures. Klaus-Jurgen Bathe, 2006.
[3] P.B. Bogert, E.D. Haugse, R.E. Gehrki, Structural shape identification from experimental strains using a modal transformation technique, in: Proceedings of 44th AIAA/ASME/ASCE/AHS Structures, Structural Dynamics and Materials Conference, Norfolk, Virginia, 2003.
[4] P. Cerracchio, M. Gherlone, M. Mattone, M. Di Sciuva, A. Tessler, Shape sensing of three-dimensional frame structures using the inverse finite element method, in: Proceedings of 5th European Workshop on Structural Health Monitoring, Sorrento, Italy, 2010.
[5] M. Chierichetti, Load and response identification for a nonlinear flexible structure subject to harmonic loads, J. Comput. Nonlinear Dyn. 9 (1) (2014) 011009.

Please cite this article in press as: A. Kefal et al., A quadrilateral inverse-shell element with drilling degrees of freedom for shape sensing and structural health monitoring, Eng. Sci. Tech., Int. J. (2016), http://dx.doi.org/10.1016/j.jestch.2016.03.006

[6] R.D. Cook, Four-node 'flat' shell element: drilling degrees of freedom, membrane-bending coupling, warped geometry, and behaviour, Comput. Struct. 50 (4) (1994) 549–555.
[7] M.A. Davis, A.D. Kersey, J. Sirkis, E.J. Friebele, Shape and vibration mode sensing using a fiber optic Bragg grating array, Smart Mater. Struct. 5 (6) (1996) 759.
[8] A. Derkevorkian, S.F. Masri, J. Alvarenga, H. Boussalis, J. Bakalyar, W.L. Richards, Strain-based deformation shape-estimation algorithm for control and monitoring applications, AIAA J. 51 (9) (2013) 2231–2240.
[9] M. Gherlone, P. Cerracchio, M. Mattone, M. Di Sciuva, A. Tessler, Beam shape sensing using inverse finite element method: theory and experimental validation, in: Proceeding of 8th International Workshop on Structural Health Monitoring, Stanford, CA, 2011.
[10] M. Gherlone, P. Cerracchio, M. Mattone, M. Di Sciuva, A. Tessler, Shape sensing of 3D frame structures using an inverse finite element method, Int. J. Solids Struct. 49 (22) (2012) 3100–3112.
[11] M. Gherlone, P. Cerracchio, M. Mattone, M. Di Sciuva, A. Tessler, An inverse finite element method for beam shape sensing: theoretical framework and experimental validation, Smart Mater. Struct. 23 (4) (2014) 045027.
[12] B. Glisic, D. Inaudi, Fibre Optic Methods for Structural Health Monitoring, John Wiley and Sons, 2008.
[13] A. Ibrahimbegovic, R.L. Taylor, E.L. Wilson, A robust quadrilateral membrane finite element with drilling degrees of freedom, Int. J. Numer. Methods Eng. 30 (3) (1990) 445–457.
[14] A. Ibrahimbegovic, E.L. Wilson, A unified formulation for triangular and quadrilateral flat shell finite elements with six nodal degrees of freedom, Commun. Appl. Numer. Methods 7 (1) (1991) 1–9.
[15] R.T. Jones, D.G. Bellemore, T.A. Berkoff, J.S. Sirkis, M.A. Davis, M.A. Putnam, A.D. Kersey, Determination of cantilever plate shapes using wavelength division multiplexed fiber Bragg grating sensors and a least-squares strain-fitting algorithm, Smart Mater. Struct. 7 (2) (1998) 178.
[16] L.H. Kang, D.K. Kim, J.H. Han, Estimation of dynamic structural displacements using fiber Bragg grating strain sensors, J. Sound Vib. 305 (3) (2007) 534–542.
[17] N.S. Kim, N.S. Cho, Estimating deflection of a simple beam model using fiber optic Bragg-grating sensors, Exp. Mech. 44 (4) (2004) 433–439.
[18] W.L. Ko, W.L. Richards, V.T. Fleischer, Applications of Ko displacement theory to the deformed shape predictions of the doubly-tapered Ikhana Wing, NASA/TP-2009-214652, 2009.
[19] P.L. Liu, H.T. Lin, Direct identification of non-uniform beams using static strains, Int. J. Solids Struct. 33 (19) (1996) 2775–2787.
[20] A. Maniatty, N. Zabaras, K. Stelson, Finite element analysis of some inverse elasticity problems, J. Eng. Mech. 115 (6) (1989) 1303–1317.
[21] A.M. Maniatty, N.J. Zabaras, Investigation of regularization parameters and error estimating in inverse elasticity problems, Int. J. Numer. Methods Eng. 37 (6) (1994) 1039–1052.
[22] M. Nishio, T. Mizutani, N. Takeda, Structural shape reconstruction with consideration of the reliability of distributed strain data from a Brillouin-scattering-based optical fiber sensor, Smart Mater. Struct. 19 (3) (2010) 035011.
[23] C.C. Quach, S.L. Vazquez, A. Tessler, J.P. Moore, E.G. Cooper, J.L. Spangler, Structural anomaly detection using fiber optic sensors and inverse finite element method, in: Proceedings of AIAA Guidance, Navigation, and Control Conference and Exhibit, San Francisco, California, 2005.
[24] D.S. Schnur, N. Zabaras, Finite element solution of two-dimensional inverse elastic problems using spatial smoothing, Int. J. Numer. Methods Eng. 30 (1) (1990) 57–75.
[25] S. Shkarayev, R. Krashantisa, A. Tessler, An inverse interpolation method utilizing in-flight strain measurements for determining loads and structural response of aerospace vehicles, in: Proceedings of 3rd International Workshop on Structural Health Monitoring, Stanford, California, 2001.
[26] S. Shkarayev, A. Raman, A. Tessler, Computational and experimental validation enabling a viable in-flight structural health monitoring technology, in: Proceedings of 1st European Workshop on Structural Health Monitoring, Cachan, Paris, France, 2002.
[27] C.W. Stoesz, Method For Analyzing Strain Data, US 8,515,675 B2, 2013.
[28] A. Tessler, T.J. Hughes, An improved treatment of transverse shear in the Mindlin-type four-node quadrilateral element, Comput. Methods Appl. Mech. Eng. 39 (3) (1983) 311–335.
[29] A. Tessler, H.R. Riggs, C.E. Freese, G.M. Cook, An improved variational method for finite element stress recovery and a posteriori error estimation, Comput. Methods Appl. Mech. Eng. 155 (1) (1998) 15–30.
[30] A. Tessler, H.R. Riggs, M. Dambach, A novel four-node quadrilateral smoothing element for stress enhancement and error estimation, Int. J. Numer. Methods Eng. 44 (10) (1999) 1527–1541.
[31] A. Tessler, J.L. Spangler, A variational principle for reconstruction of elastic deformation of shear deformable plates and shells, NASA TM-2003-212445, 2003.
[32] A. Tessler, J.L. Spangler, Inverse FEM for full-field reconstruction of elastic deformations in shear deformable plates and shells, in: Proceedings of 2nd European Workshop on Structural Health Monitoring, Munich, Germany, 2004.
[33] A. Tessler, J.L. Spangler, A least-squares variational method for full-field reconstruction of elastic deformations in shear-deformable plates and shells, Comput. Methods Appl. Mech. Eng. 194 (2) (2005) 327–339.
[34] A. Tessler, J.L. Spangler, M. Gherlone, M. Mattone, M. Di Sciuva, Real-time characterization of aerospace structures using onboard strain measurement technologies and inverse finite element method, in: Proceedings of the 8th International Workshop on Structural Health Monitoring, Stanford, California, 2011.
[35] A.N. Tikhonov, V.Y. Arsenin, Solutions of Ill-posed Problems, Winston, Washington, DC, 1977.
[36] S. Timoshenko, J.N. Goodier, Theory of Elasticity, McGraw-Hill, New York, 1951.
[37] S.L. Vazquez, A. Tessler, C.C. Quach, E.G. Cooper, J. Parks, J.L. Spangler, Structural health monitoring using high-density fiber optic strain sensor and inverse finite element methods, NASA TM-2005-213761, 2005.

Please cite this article in press as: A. Kefal et al., A quadrilateral inverse-shell element with drilling degrees of freedom for shape sensing and structural health monitoring, Eng. Sci. Tech., Int. J. (2016), http://dx.doi.org/10.1016/j.jestch.2016.03.006